buildings

MDPI

Article

Carbonation Performance and Characterization of Alkali-Activated Cementitious Materials Incorporating Superabsorbent Polymers

Wanguo Zhang [1], Yunjuan Chen [2,3,*], Yuanshun Xiong [1], Yichen Zhang [2,3], Yuanhui Qiao [1], Quansheng Sun [1] and Zhen Wang [2,3]

[1] China Railway 14th Bureau Group Co., Ltd., Jinan 250014, China; 15065821592@163.com (W.Z.); 15650325795@163.com (Y.X.); 15854933130@163.com (Y.Q.); 17390349319@163.com (Q.S.)
[2] School of Civil Engineering, Shandong Jianzhu University, Jinan 250101, China; 15665898783@163.com (Y.Z.); wangzhen@sdjzu.edu.cn (Z.W.)
[3] Key Laboratory of Structural Reinforcement and Underground Space Engineering, Ministry of Education, Jinan 250101, China
* Correspondence: skdcyj@126.com

Abstract

To effectively mitigate the early-age shrinkage and cracking of alkali-activated cementitious materials (AAMs), superabsorbent polymers (SAPs) were adopted in this study to absorb and store water in the mixture, which is continuously released during the setting and hardening process. This approach prolongs the setting and hardening process of AAM, improves the stability of its microstructure, and reduces crack formation. Meanwhile, the influence mechanism of CO_2 curing on the strength of SAP-modified AAM was investigated. Through mechanical strength testing, X-ray diffraction (XRD), thermogravimetric analysis (TGA), heat release measurement during setting and hardening, and pore size distribution testing of specimens with different mix proportions and curing conditions, effective methods to improve the mechanical strength and microstructural development of AAM were explored. The results show that CO_2 curing can significantly enhance the early-age strength of AAM, promote the formation of carbonation products, and optimize the pore structure of AAM at the micro-level. An appropriate amount of SAP can prolong the setting and hardening process of AAM and improve the degree of its setting and hardening; however, excessive SAP reduces the concentration of alkaline solution in the mixture matrix, increasing resistance to the setting and hardening of AAM.

Keywords: CO_2 curing; alkali-activated cementitious materials; superabsorbent polymer; microstructural characterization

Check for updates

Academic Editor: Mauro Mitsuuchi Tashima

Received: 23 March 2026
Revised: 24 April 2026
Accepted: 27 April 2026
Published: 30 April 2026

Copyright: © 2026 by the authors. Licensee MDPI, Basel, Switzerland. This article is an open access article distributed under the terms and conditions of the Creative Commons Attribution (CC BY) license.

1. Introduction

Portland cement, as the most widely used basic building material in the world, consumes massive energy for its production, which results in excessive greenhouse gas emissions during its production and application. The process of cement production accounts for approximately 7–8% of global anthropogenic CO_2 emissions [1]. Alkali-activated cementitious materials (AAMs) have been studied as a class of green cementitious materials since the early 20th century, with early developments by Purdon in the 1930s and systematic investigations by Glukhovsky and Krivenko in the 1950s–60s in the former Soviet Union [2]. AAM typically exhibits fast hardening, early strength and excellent corrosion resistance.

Generally, AAMs are manufactured by the reaction of industrial solid wastes (such as slag, fly ash, red mud, etc.) with alkaline solutions (such as NaOH solution, sodium silicate solution, etc.) as activators at room temperature. According to the calcium content of the precursors, AAMs are generally classified into two categories, i.e., high-calcium systems (e.g., slag-based) and low-calcium systems (e.g., low-calcium fly ash-based) [3]. High-calcium systems primarily form calcium aluminosilicate hydrate (C-A-S-H) gels, whereas sodium aluminosilicate hydrate (N-A-S-H) gels are the main products in low-calcium systems. The carbon emissions generated during the preparation of AAM can be significantly lower than those of ordinary Portland cement (OPC), with reported reductions ranging from approximately 40% to 80% depending on the precursor type, activator composition, dosage, and system boundaries considered in the life cycle assessment [4]. Compared to cement-based cementitious materials, AAMs adopting slag-activated and sodium silicate or sodium hydroxide typically exhibit a faster setting and hardening rate and can achieve higher strength within a shorter curing time [5–7]. However, the setting behavior and early strength development of AAMs are highly dependent on the precursor composition and activator type; for instance, slag systems activated with calcium-based activators may exhibit prolonged setting times and relatively low early strength [8].

The superabsorbent polymer (SAP) is a polyelectrolyte with a cross-linked structure, which can absorb and store water dozens or even hundreds of times its own mass, and release the water into the surrounding environment during the solidification of the paste [9]. SAP is applied as an internal curing agent in the raw materials of AAM, so that it absorbs and stores water during the production and mixing process, and gradually releases it during the setting and hardening process, optimizing the early internal curing environment, thus prolonging the setting and hardening time of AAMs and deepening the degree of setting and hardening [10]. However, it should be noted that SAP desorption also leads to the formation of macroscopic voids within the hardened matrix, which can alter the pore structure and potentially affect the mechanical performance and pore characteristics of AAMs [11].

In this process, high-concentration CO_2 diffuses into the matrix through the pores on the surface of AAM, dissolves in the pore solution, and reacts with a large number of free cations such as Na^+, Mg^{2+} and Ca^{2+} in the pore solution to generate sodium salts (e.g., Na_2CO_3, which is highly soluble) and sparingly soluble phases such as $MgCO_3$ and $CaCO_3$ precipitates [12]. It is well established that the $CaCO_3$ microcrystals generated by CO_2 curing can significantly improve the early-age strength of concrete, as well as its durability such as resistance to chloride ion penetration, sulfate attack and freeze–thaw damage [13–15]. However, other studies have indicated that under certain conditions, the carbonation process can alter the pore structure of AAM, reduce the pH value of the pore solution, and may contribute to the deterioration of mechanical and durability properties, particularly when the pH decreases below the threshold required for the stability of the binding gel phases [16–18]. The extent of such degradation depends on factors including the calcium content of the system, the CO_2 concentration, and the exposure duration. The huge difference in the above results is due to the different calcium contents in the raw materials. The setting and hardening products of AAM are usually divided into two categories: one is mainly made of slag, and the main component of the product is calcium aluminosilicate hydrate (C-A-S-H) gel; the other is mainly made of raw materials with low calcium content such as low-calcium fly ash, and a solid compound with sodium aluminosilicate hydrate (N-A-S-H) gel is the main product generated [19–22]. During the CO_2 curing of AAM, CO_2 first dissolves in the pore solution to form carbonic acid, which dissociates into carbonate (CO_3^{2-}) and bicarbonate (HCO_{3-}) species. These species then interact with dissolved cations (e.g., Na^+, Ca^{2+}, and Mg^{2+}) present in the pore solution and

may precipitate as carbonate phases (e.g., $CaCO_3$ and Na_2CO_3), resulting in a decrease in the pH value of the pore solution [23]. When a significant number of alkaline cations in the pore solution are consumed by CO_2, the structural integrity of the AAM matrix is compromised [24,25]. In AAMs with high calcium content, when the pH of the pore solution decreases to values below approximately 10–11, the original C-A-S-H gel products undergo progressive decalcification, leading to partial decomposition of the gel network. It should be noted that unreacted slag particles can act as a reservoir of Ca^{2+}, providing a buffering effect that partially mitigates the extent of decalcification [26]. However, the further formation of $CaCO_3$ crystal precipitation can fill the pores. Therefore, a small amount of decalcification reaction does not cause the loss of mechanical strength of AAM. With the deepening of the carbonation reaction, its mechanical strength may change significantly, which needs further research and confirmation. In the system dominated by N-A-S-H gel, there is no decalcification reaction in the skeleton, and the precipitation of $CaCO_3$ crystals is not obvious. However, in a high-concentration CO_2 environment, the combined effects of $MgCO_3$ and Na_2CO_3 formation on the microstructural evolution and long-term performance of AAM remain insufficiently understood. This study aims to address this gap by systematically investigating the interaction between CO_2 curing and SAP incorporation in a slag–fly-ash-blended AAM system.

In this study, fly ash and slag were used as mixed raw materials at a mass ratio of 1:1. This precursor combination was selected to achieve a moderate calcium content in the system (Ca/(Si + Al) ≈ 0.68), which allows for the coexistence of both C-A-S-H and N-A-S-H gels. Such a blended system provides a representative platform to investigate the interplay between internal curing (via SAP) and CO_2 curing, as both high-calcium and low-calcium characteristics are present. AAM mix proportions with different SAP contents were designed. Meanwhile, the influence mechanisms of standard curing and CO_2 curing on the setting and hardening process of AAM were compared to explore effective methods to optimize the mechanical strength and microstructural development of AAM.

2. Experimental Methods

2.1. Material Preparation

S95-grade slag was selected in the experiment, and its technical indicators were tested in accordance with the Test Method for Fineness of Mineral Admixtures (GB/T 27973-2011) [27]. Its specific surface area was 400 m^2/kg, the moisture content was less than 1%, and the activity index at 28 days was more than 95%. All indicators met the standards, and their application conditions complied with the technical specifications of Mineral Admixtures for Concrete (GB/T 18046-2008) [28].

Class I fly ash was used in the experiment, and its application indicators were tested in accordance with Fly Ash for Cement and Concrete (GB 1596-2017) [29]. The fineness was 11.9%, the water demand ratio was lower than 94%, the loss on ignition was less than 5%, and the sulfur trioxide content was lower than 1%. All indicators met the national standards. The chemical compositions of fly ash and slag are shown in Table 1.

Table 1. Main chemical components (wt.%).

Composition	CaO	SiO_2	Al_2O_3	MgO	SO_3	TiO_2	Fe_2O_3	K_2O	MnO
Fly Ash	5.29	47.18	30.07	0.51	1.90	1.53	11.20	0.99	0.05
Slag	43.26	30.62	14.07	6.09	2.36	0.68	0.71	0.46	0.36

The sodium hydroxide powder used in the experiment was provided by Foshan Xilong Chemical Co., Ltd., Foshan, Guangdong, China, with a purity of 99%. The sodium silicate solution was produced by Jiashan County Yourui Refractory Material Co., Ltd., Jiaxing,

Zhejiang, China. It has a Na_2O content of 8.53% (mass fraction), a solid–liquid mass ratio of 0.35:0.65 and a modulus of 3.3.

The internal curing material used in the experiment was low-cross-linking polyacrylic acid-based SAP spherical particles, produced by Gongyi Meiyuan Water Purification Material Co., Ltd., Gongyi, Henan, China.The main component of the SAP is sodium polyacrylate, the water absorption rate of which in deionized water can reach 400 g/g within 30 min, showing characteristics of fast water absorption and strong water retention. The particle size range of the dry particles is 0.42~0.6 mm, which does not affect the flow state during stirring when used to prepare AAM.

2.2. Specimen Preparation

This paper aims to study the effects of standard curing and CO_2 curing environments on the micro-products and structures of AAM after adding different amounts of admixture SAP; it also aims to explore the change mechanisms of these two factors on the mechanical performance and pore structure evolution of AAM after setting and hardening. To prevent SAP from absorbing water too fast at the initial stage of stirring, which leads to the premature loss of fluidity and uneven stirring of AAM paste, the water-to-binder ratio of AAM was designed to be 0.3. Fly ash and slag were used as the main raw materials at a mass ratio of 1:1 to provide mechanical strength after setting and hardening, while preventing an excessively high calcium content in the system, which could adversely affect the CO_2 curing effect. The alkali activator solution was prepared by mixing NaOH solution and sodium silicate solution in a certain proportion, with a modulus of 1.0 and an OH^- concentration of 4.0 mol/L.

Specimens under standard curing were placed in a standard curing box with a temperature of 20 ± 2 °C and a humidity of 95% for curing, demolded after 24 h, and continued to be cured to the specified age under the same conditions. Specimens were cured in the environment with a constant temperature (20 ± 2 °C), humidity (95%), and a CO_2 concentration at 20% to the same age. This CO_2 concentration was selected to accelerate the carbonation process and significantly alter the microstructural and mechanical changes within a practical experimental timeframe, consistent with accelerated carbonation testing protocols commonly employed in the literature [30]. The control conditions in the experimental design are shown in Table 2.

Table 2. Mix proportions of AAM paste.

Test No.	w/b *	Slag/FA	NaOH (mol/L)	Na_2O/SiO_2	SAP/Slag+FA(wt%)	SAP Free Swell Capacity(g/g)	Curing Method
A0S	0.3	1	4.0	1.0	0	551	Standard curing
A5S	0.3	1	4.0	1.0	0.05	551	Standard curing
A20S	0.3	1	4.0	1.0	0.2	551	Standard curing
A40S	0.3	1	4.0	1.0	0.4	551	Standard curing
A0S-C	0.3	1	4.0	1.0	0	551	CO_2 curing
A5S-C	0.3	1	4.0	1.0	0.05	551	CO_2 curing
A20S-C	0.3	1	4.0	1.0	0.2	551	CO_2 curing
A40S-C	0.3	1	4.0	1.0	0.4	551	CO_2 curing

* w/b refers to the water–binder ratio of the specimen.

In the preparation process of specimens, the alkali activator solution was first prepared: the sodium hydroxide particles, weighed according to the mixed proportion, were added to laboratory pure water and then mixed with the sodium silicate solution until the modulus of the mixed solution was 1.0. Slag and fly ash in the specified proportion were added to the mixing bowl and stirred at a low speed for 30 s to mix evenly; then, SAP was added

and stirred at a low speed for another 30 s to disperse it fully and evenly. The prepared alkali activator solution was added, stirred at a low speed until the mixture was completely and evenly mixed, and then stirred at a high speed for 30 s. After mixing, the mixture was poured into a cuboid mold of 40 mm × 40 mm × 160 mm, subject to vibration on a vibration table for about 20 s to remove air bubbles, and then the surface was troweled, covered with plastic wrap to prevent water evaporation, and placed under the designed curing conditions until the experimental age was reached.

2.3. Experimental Design

The flexural strength and compressive strength of the specimens were tested at 7 days and 28 days under standard curing and CO_2 curing, respectively. The SANS compressive and flexural-integrated testing machine (300 kN) was used in the laboratory, and the test was carried out in accordance with the Test Method for Strength of Cement Mortars (ISO Method). Three samples were tested for flexural strength in each group: the specimen was placed on support columns with a span of 100 mm, the long axis of the specimen was perpendicular to the support columns, the loading rate was 50 N/s ± 10 N/s, and the load was applied vertically in the middle of the specimen until fracture. For the compressive strength test, 6 fractured specimens from the flexural strength test were selected, the loading rate of the testing machine was 2400 N/s ± 200 N/s, and the pressing area was 1600 mm^2.

The non-surface parts of the broken AAM test blocks after mechanical tests were selected, ground into powder, sieved with an 80-mesh sieve, and the powder was collected for further microstructural characterization and analysis. For microstructural and thermal analyses (XRD, TGA, and MIP), representative samples extracted from the crushed cores of the mechanical test specimens were utilized. The analytical curves presented herein denote the representative behavior confirmed through duplicate experimental runs to ensure data reliability. Furthermore, in the graphical representations of mechanical performance (Figures 1 and 2), the error bars explicitly represent the standard deviation derived from the replicate specimens tested for each mix proportion (three replicates for flexural strength and six for compressive strength). XRD technology was used for qualitative analysis of the crystal types of AAM products. The relevant equipment was a Smart lab series XRD analyzer produced by Rigaku, Japan, with a scanning range of 5°~80°, a scanning speed of 2°/min and a step size of 0.02°.

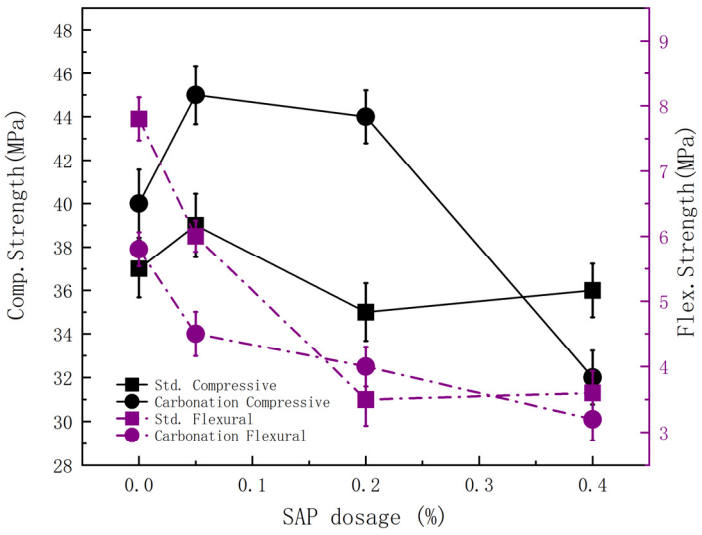


Figure 1. Mechanical properties of specimens at 7 days of age.

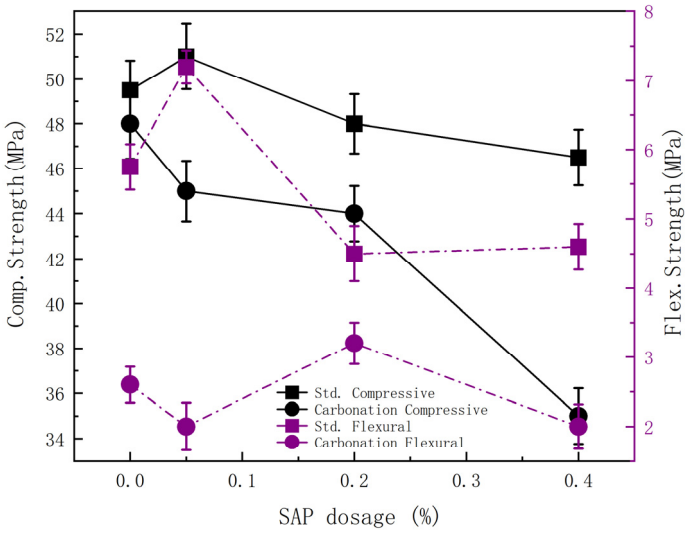


Figure 2. Mechanical properties of specimens at 28 days of age.

Thermogravimetric analysis (TGA) was carried out with an STA 449 instrument manufactured by Netzsch Gerätebau GmbH, Selb, Bavaria, Germany. The types and relative contents of various products in AAM were inferred by detecting the change in sample mass with temperature. The AAM sample was ground and sieved with a 200-mesh sieve to ensure that the sample particles were fine and uniform, and 20 mg was taken as the test sample. The heating environment was nitrogen, the heating temperature was 20~800 °C, the heating rate was 10 °C/min, and an open alumina (Al_2O_3) crucible was used as the container.

The isothermal calorimeter TAM Air was used to detect the heat release phenomenon of AAM with different SAP contents during setting and hardening, record the heat flow in the first 72 h of the setting and hardening process and the cumulative heat release in 240 h. The data were recorded once per second in the first 10 min and once per minute thereafter to explore the influence of SAP on the setting and hardening reaction of AAM.

In addition, mercury intrusion porosimetry (MIP) was used to test the pore size distribution of AAM after carbonation for 28 d with different SAP contents. The test instrument was an AutoPore V 9600 fully automatic mercury intrusion porosimeter manufactured by Micromeritics Instrument Corporation, Norcross, GA, USA, with a pore size measurement range of 0.003–1100 μm.

3. Results and Analysis

3.1. Changes in Mechanical Properties of SAP-AAM Under Different Curing Methods

Figure 1 shows the mechanical strength test results of AAM specimens with different SAP contents under standard curing and CO_2 curing at 7 days of age. It can be seen that, in terms of compressive strength, except for A40S specimens, the strength of specimens under CO_2 curing is higher than that under standard curing at the same SAP content, with a general strength increase rate of more than 9%. Among them, the compressive strength of A20S specimens is the most significantly improved, with a maximum increase of 26% after CO_2 curing. Contrary to the change in compressive strength, CO_2 curing leads to a significant decrease in the flexural strength of specimens. Among them, the flexural strength of AAM specimens without SAP decreases by more than 26% after CO_2 curing, while the loss of flexural strength caused by CO_2 curing is reduced after adding the SAP admixture, and the higher the SAP content, the less the flexural strength is affected by CO_2. This observation is consistent with previous studies showing that during CO_2 curing, the precipitation of $CaCO_3$ crystals within the pore network and microcracks can densify the

microstructure, thereby improving the load-bearing capacity under compression [14]. The reduction in flexural strength, however, may be attributed to the partial decalcification of the calcium aluminosilicate hydrate gel, which reduces the toughness of the binding matrix. However, the carbonation reaction itself reacts with the calcium aluminosilicate hydrate gel in the specimen, which is hypothesized to cause partial decalcification of the gel and modification of the binding network, potentially leading to a decrease in the toughness of the material and, thus, a decrease in flexural strength [31,32].

With the increase in SAP content, the compressive strength of all specimens first increases and then decreases. When the content is 0.05%, the compressive strength of the specimen can reach 45 MPa, and the flexural strength is 4.5 MPa. When the SAP content increases to 0.2%, the compressive strength of the specimen is 44 MPa, and the flexural strength is 4 MPa, with a small change range. However, with the further increase in SAP content, the mechanical strength of AAM decreases significantly, indicating that SAP has a negative effect on the mechanical properties of AAM. This is because during the setting and hardening process of AAM, excessive SAP absorbs liquid and swells, exerting pressure on the surrounding matrix. With the development of the setting and hardening process, SAP releases liquid and shrinks, resulting in irreparable holes inside the gel matrix, which ultimately has a negative impact on the mechanical strength of AAM [33].

Figure 2 shows the mechanical properties of AAM with different SAP contents at 28 days of age under standard curing and CO_2 curing. The 7-day compressive strength of all AAM specimens exceeded more than 70% of the 28-day compressive strength, which is consistent with the characteristic of the fast early-age strength growth of AAM, indicating that the addition of SAP has little effect on the early-age strength growth of AAM. The compressive strength of specimens under CO_2 curing has very limited growth from 7 days to 28 days, and the strength of AAM remains unchanged when the SAP content is 0.05% and 0.2%. Under standard curing conditions, the compressive strength of all specimens increases by more than 20% from 7 days to 28 days of age, and the specimen with the highest compressive strength is A5S, with a value of 51 MPa. For specimens with the same mix proportion under CO_2 curing, the 28-day compressive strength decreases by 3%~24%. The above results show that CO_2 curing can improve the early-age strength growth rate of AAM, but has a negative impact on the 28-day strength of AAM specimens. The limited strength development under CO_2 curing may be associated with the moderate calcium content of the blended system (Ca/(Si + Al) = 0.68), which favors the formation of N-A-S-H as a major binding phase. In the systems, the amount of $CaCO_3$ precipitation available to fill pores and enhance strength is relatively low compared to high-calcium slag-based systems, as reported in previous studies on the carbonation behavior of blended AAM [34]. In addition, with the increase in SAP content beyond 0.05%, the compressive strength of the specimens decreases, especially for the specimens under CO_2 curing, the 28-day compressive strength of which decreases by a maximum of 27%. This is mainly due to the fact that excessive SAP absorbs liquid at the initial stage of setting and releases liquid after setting and hardening, but this liquid absorption and release behavior increases the pore volume and pore solution content in AAM, making the inlet and outlet channels of high-concentration CO_2 more extensive, the amount of CO_2 absorbed by the pore solution larger, and the alkalinity lower.

Under standard curing conditions, with the increase in SAP content, the flexural strength of specimens A5S, A20S and A40S increases by 20%, 29% and 28%, respectively, from 7 days to 28 days of age, indicating the strength compensation effect of SAP on AAM. However, under CO_2 curing conditions, the flexural strength of all specimens loses more than 20% from 7 days to 28 days, and its negative effect is consistent with the performance of

compressive strength, which is mainly related to the voids formed after the water absorbed by SAP is released into the cementitious material matrix.

3.2. Crystallization Changes in SAP-AAM Under Different Curing Methods

The XRD analyses of SAP-AAM under different curing methods are shown in Figure 3. A broad diffuse halo appears at 20–35° 2θ range and is identified as poorly crystalline binding phases in AAM. In the slag–fly-ash-blended system investigated here, this feature reflects contributions from both calcium aluminosilicate hydrate (C-A-S-H) and sodium aluminosilicate hydrate (N-A-S-H) gels. The absence of sharp Bragg reflections in this region confirms the predominantly amorphous nature of the main reaction products [35]. In Figure 3b, the diffuse scattering feature in the 20–35° 2θ range appears more defined, which can indicate an increase in the degree of short-range ordering within the amorphous gel phases. This evolution is consistent with the progressive development of the binding matrix over time. With the progress of the curing process, the "hump peak" becomes sharper, which means that the order of the amorphous gel increases. This is also a superimposed signal peak, and its sharp part comes from the strong peak of newly generated crystals with higher crystallinity. Zhao et al. [36] reported that during CO_2 curing, the main crystalline carbonate product generated by calcium-containing cementitious materials is calcium carbonate ($CaCO_3$), which may precipitate in three different polymorphic forms: calcite, aragonite and vaterite. Calcite is the most thermodynamically stable phase under ambient conditions. Therefore, the evolution of the XRD pattern in this region may be attributed, at least in part, to the formation of carbonate phases (such as calcite) resulting from the carbonation process. However, it should be noted that the identification of carbonate phases based solely on the diffuse scattering feature at 20–35° 2θ is inconclusive, as this region does not contain the primary diagnostic reflections for calcite (which typically appear at 29.4° 2θ) or other $CaCO_3$ polymorphs. Further evidence from TGA is required to confirm the presence and quantity of carbonate phases [37]. SAP is an inert material in alkali-activated cementitious materials, so it cannot change the types of crystalline substances in the cementitious material system. The peaks of quartz and mullite in fly ash are also reflected in the pattern. During the setting and hardening process of AAM, these two types of crystals do not directly participate in the reaction and only act as fillers in the gel products [38].

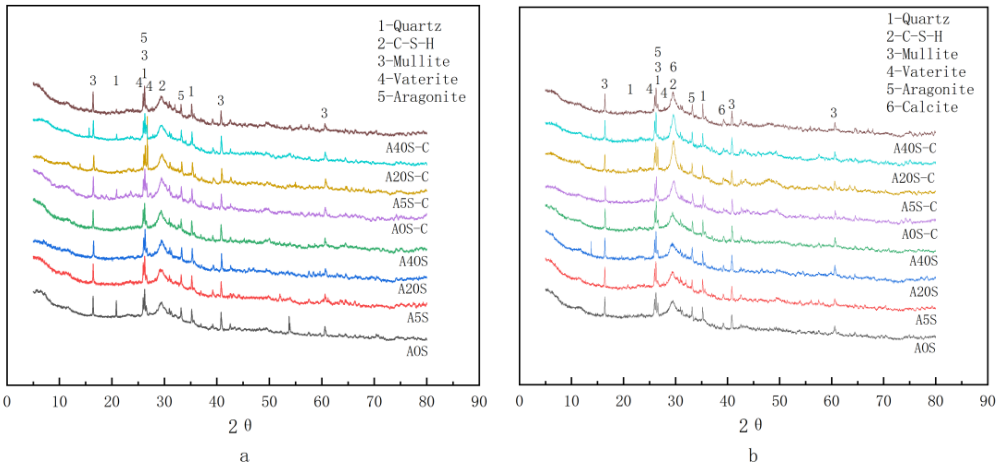


Figure 3. XRD analysis before and after carbonation: (**a**) XRD pattern at 7 days; (**b**) XRD pattern at 28 days.

3.3. Changes in Phase Composition of SAP-AAM Under Different Curing Conditions

Figure 4 shows the thermogravimetric curves before and after carbonation, in which Figure 4a,b show the curves of mass loss with temperature rise at 7 days and 28 days of age, respectively, and Figure 4c,d show the weight loss rates of specimens under standard curing and carbonation curing at 28 days of age, respectively. Marjia et al. [39] summarized the weight loss temperatures of various substances during alkali-activated thermogravimetric analysis, and the decomposition of the main analyzed substances in each temperature range is marked in the figure. Free water molecules in the matrix are mainly within 105 °C, and the main mass loss within 245 °C is from the loss of bound water in C-A-S-H and N-A-S-H gels. Soluble carbonates decompose between 110 °C and 180 °C, the weight loss temperature of amorphous carbonates is generally between 250 °C and 600 °C, and the weight loss temperature of crystalline carbonates is higher, between 640 °C and 750 °C.

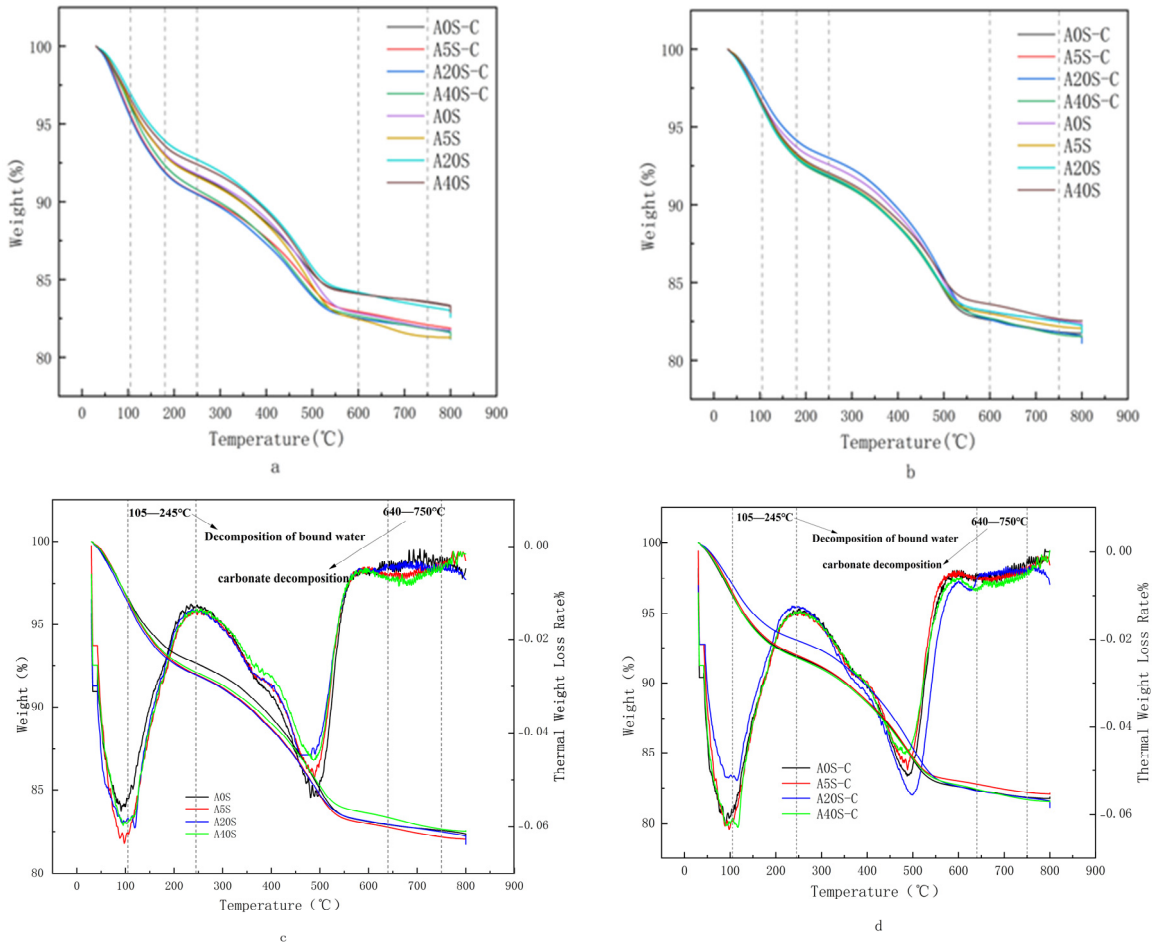


Figure 4. Thermogravimetric analysis before and after carbonation: (**a**) thermogravimetric analysis at 7 days; (**b**) thermogravimetric analysis at 28 days; (**c**) DTG curve of standard curing at 28 days; (**d**) DTG curve of carbonation curing at 28 days.

Analysis from the thermogravimetric data shows that when the temperature reaches 800 °C, the loss on ignition of specimen A5S is the largest at 7 days of age. At 28 days of age, the mass loss of A0S is about 18%, and that of A0S-C is about 19%, and the loss on ignition of specimens under CO_2 curing is higher than that under standard curing. This is because with the extension of curing time, the decalcification reaction of calcium aluminosilicate hydrate intensifies, carbonate products accumulate continuously, and the mass loss in 640 °C–750 °C increases, making the total loss on ignition of specimens under CO_2 curing generally higher than that under standard curing. It should be noted that at

28 days, the mass loss upon heating of A5S and A20S specimens is higher than that of A0S. This observation is consistent with the hypothesis that an appropriate amount of SAP promotes the continued reaction of the precursors through internal curing, resulting in a greater quantity of hydrated gel phases that contribute to the mass loss in TG. However, quantitative analysis of the TG data is needed to confirm this interpretation [40–42].

It can be seen from Figure 4c that for both specimens under CO_2 curing and standard curing, the most obvious weight loss rate peaks appear at about 100 °C and 500 °C, corresponding to the decomposition of gel and carbonate, respectively. Among them, at about 100 °C, the peak of specimen A5S is the highest, indicating that the decomposition of its amorphous gel is more prominent, which is consistent with the test results of material mechanical properties, strongly indicating the promoting effect of the 0.05% SAP dosage on the formation of amorphous gel products. At 500 °C, the specimens after CO_2 curing show a stronger peak, confirming the production of carbonate substances in a high-concentration CO_2 environment. The bound water content was estimated from the mass loss between 105 °C and 245 °C, while the carbonate content was estimated from the mass loss between 640 °C and 750 °C. The results indicate that A5S specimens exhibit approximately 13.6% higher bound water content compared to A0S, and CO_2-cured specimens show approximately 41.2% higher carbonate content compared to standard-cured specimens. These quantitative estimates support the interpretation that SAP (at optimal dosage) promotes gel formation, while CO_2 curing enhances carbonate precipitation. It can be seen from Figure 4c that the mass loss of specimens after CO_2 curing at 300 °C is greater than that of specimens under standard curing, and the mass loss here is mainly caused by the decomposition of amorphous carbonates. At 600 °C, the specimens under CO_2 curing show an endothermic decomposition peak, which is consistent with the XRD analysis results, fully illustrating the production of calcite after the decalcification reaction of C-A-S-H.

3.4. Heat Release Changes in SAP-AAM During Setting and Hardening

Since the isothermal calorimeter has uniform requirements for the ambient temperature and humidity during use, the heat release and heat flow of AAM mixed with SAP under a standard environment were detected. By comparing the alkali-activated setting and hardening heat release rate and cumulative heat release of each group of samples, the influence of SAP on the heat release during the setting and hardening process of AAM was mainly analyzed, and the results are shown in Figure 5. Under identical environmental and testing conditions, the same batch of specimens was used in isothermal calorimetry experiments. The heat flow curve reflects the instantaneous heat release rate. As the reaction rate decays to near zero within the first 72 h (i.e., the heat flow peak essentially ends), rate monitoring for only 72 h suffices to obtain complete kinetic information. In contrast, the cumulative heat release is obtained by integrating the entire heat flow curve over time; this requires the integration to stabilize (i.e., no further significant increase), necessitating continuous measurement up to 240 h to determine the accurate total heat release. Thus, although the two measurements differ in duration, their data originate from the same specimens and conditions.

It can be seen from Figure 5a that AAM shows two heat release peaks in terms of heat release rate. The first heat release peak reaches the highest point at about 1 h, which is caused by the dissolution of slag after being activated by the alkaline activator. Then it enters the induction period of the setting and hardening process, during which the heat release rate decreases. With the progress of the reaction, a second heat release peak appears, which is caused by the gel products generated by the violent setting and hardening reaction of slag. In the specimens of A5S and A20S, it can be seen that the induction period of the heat release reaction is prolonged compared with the blank group specimens, the main heat

release peak is delayed, and the heat release peak of setting and hardening shifts slightly to the right [43]. From the heat flow curves, the following parameters were extracted: induction period duration, time to the main heat release peak, peak heat flow value, and cumulative heat release at 72 h and 240 h. The results show that the induction period of A5S is prolonged by approximately 5.8% compared to A0S, and the time to the main heat release peak is delayed by 1.2 h. The cumulative heat release of A5S at 240 h is approximately 7.6% higher than that of A0S, confirming the beneficial effect of optimal SAP dosage on the overall degree of reaction. This is because after adding SAP, the dry SAP particles quickly absorb a part of the alkali activator solution, making the initial amount of free alkaline solution participating in the reaction relatively reduced, thus slowing down the initial reaction rate and leading to a longer induction period and a later heat release peak. At the same time, it can be seen that the peak value of the main heat release peak is reduced, which is also due to the initial decrease in alkaline solution content because part of the alkaline solution is absorbed by SAP.

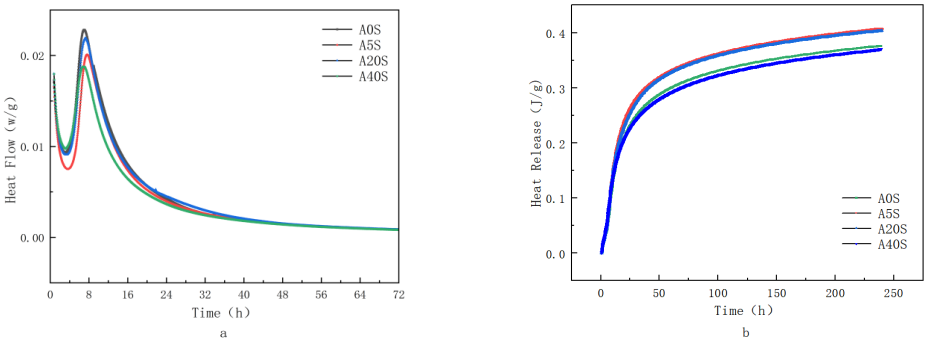


Figure 5. Heat release curves with different SAP contents: (**a**) heat release rate curve; (**b**) cumulative heat release curve.

In terms of cumulative heat release, the cumulative heat from the reaction of A5S and A20S is higher than that of the blank group. This observation is consistent with the internal curing mechanism proposed in previous studies, whereby SAP gradually releases the absorbed alkaline solution over time, allowing continued reaction of unreacted precursor particles and resulting in a higher total heat release [44]. At the same time, it is also noted that the cumulative heat release of A40S specimens is lower than that of the blank group, which is because too much SAP is added, and too much alkaline solution is absorbed at the initial stage of the reaction, resulting in the abnormal progress of the setting and hardening reaction, thus reducing the overall heat release during setting and hardening.

3.5. Pore Size Distribution Analysis of SAP-AAM

Figure 6 shows the pore size distribution curve of specimens under CO_2 curing at 28 days of age obtained by MIP analysis, including the threshold pore diameter, the most probable pore diameter, the cumulative pore volume, and the pore volume fraction in different size ranges (gel pores: <10 nm, capillary pores: 10–100 nm, and macropores: >100 nm). The results show that the A5S-C specimen exhibits the smallest threshold pore diameter (13.6 nm) and the lowest cumulative pore volume (0.0172 mL/g) among all specimens, confirming the pore-refining effect of the optimal SAP dosage combined with CO_2 curing. In contrast, A40S-C shows a significant increase in the fraction of macropores (>100 nm), which correlates with the observed reduction in compressive strength. It can be seen from the figure that the pore size of both the blank group and the specimens with SAP is mainly concentrated in the range of 10–100 nm, which belongs to the category of capillary pores. With the increase in SAP content, the most probable pore size of the specimens shows a trend of first decreasing and then increasing. Among them, the peak

of the A5S-C specimen is slightly to the left of the A0S-C specimen, which indicates that its most probable pore size is the smallest and the cumulative pore volume is lower than that of other specimens, indicating that 0.05% SAP content can effectively refine the pore size. SAP releases the stored water in the later stage of setting and hardening, promotes the continuous reaction of unreacted particles, and generates more gel to fill the pores, thus making the pore structure denser [33,42]. Meanwhile, calcium carbonate precipitation generated by CO_2 curing may further fill the capillary pores and contribute to the refinement of the pore size distribution.

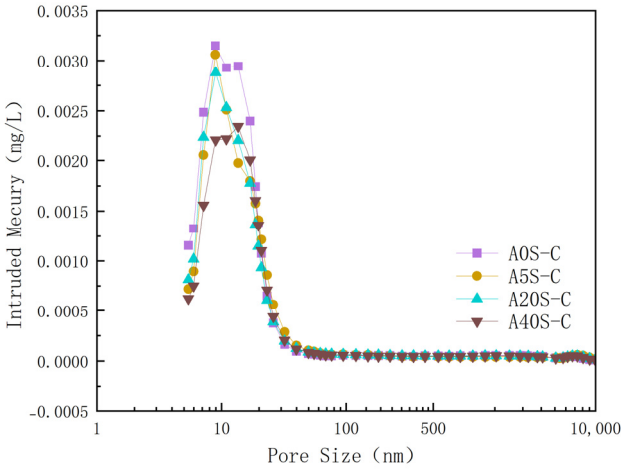


Figure 6. Pore size distribution of specimens under CO2 curing at 28 days of age.

When the SAP content increases to 0.4%, the most probable pore size of the specimen increases significantly, and the cumulative pore volume rises remarkably. This is because excessive SAP absorbs water and swells at the initial stage of setting, forming a large, reserved space in the matrix; it leaves voids that cannot be completely filled by gel after water release and shrinkage in the later stage, resulting in an increase in the proportion of large pores. It is worth noting that although the most probable pore size of the A20S-C specimen is higher than that of A5S-C, its compressive strength is the most significantly improved at 7 days (see Figure 1). This may be because the existence of an appropriate amount of large pores provides a more extensive diffusion channel for CO_2, promoting the early carbonation reaction and the rapid formation of calcium carbonate and thus making up for some pore defects in the early stage [45].

3.6. Summary of Optimal SAP Performance

To elucidate the underlying mechanisms of the optimal SAP dosage, Table 3 consolidates the critical mechanical, thermal, and microstructural parameters for the baseline (A0S) and optimal (A5S) mixtures.

Table 3. Summary of optimal SAP performance parameters.

Parameter	Baseline (A0S/A0S-C)	Optimal 0.05% SAP (A5S/A5S-C)
7 d Compressive Strength (Std/CO_2)	37 MPa/40 MPa	39 MPa/45 MPa
28 d Compressive Strength (Std/CO_2)	49.5 MPa/48 MPa	51 MPa/45 MPa
7 d Flexural Strength (Std/CO_2)	7.8 MPa/5.8 MPa	6 MPa/4.5 MPa
28 d Flexural Strength (Std/CO_2)	5.75 MPa/2.6 MPa	7.2 MPa/2 MPa
Induction Period Duration	Baseline	+5.8% increase
Time to Main Heat Release Peak	Baseline	Delayed by 1.2 h
240 h Cumulative Heat Release	Baseline	+7.6% increase
28 d Threshold Pore Diameter (CO_2)	15 nm	13.6 nm (Refined)

4. Conclusions

In this paper, the effects of CO_2 curing and internal SAP addition on the mechanical strength, setting and hardening mechanisms of AAM were studied by means of mechanical testing, microstructural characterization and detection. The results show that when the SAP content is more than 0.2%, the water absorbed and released by SAP leads to an increase in voids in the AAM matrix and a decrease in mechanical properties, which is not conducive to the setting and hardening reaction of AAM. In this experiment, when the SAP content is 0.05%, both the compressive strength and flexural strength of AAM are enhanced, and the results of microstructural characterization and detection show that this SAP content has a promoting effect on the setting and hardening process of AAM. The influence of CO_2 curing conditions on AAM is much greater than the modification effect of SAP addition on AAM. MIP and thermal analysis suggest that while CO_2 curing induces $CaCO_3$ precipitation, this process may simultaneously alter the gel skeleton. The resulting pore structure modifications, particularly the coarsening observed at higher SAP dosages, appear to correspond with the variations in mechanical performance.

Author Contributions: Conceptualization, W.Z.; Methodology, Y.C.; Resources, Y.Q.; Writing—original draft, Y.X. and Y.Z.; Writing—review and editing, Z.W.; Visualization, Q.S. and Z.W. All authors have read and agreed to the published version of the manuscript.

Funding: This research received no external funding.

Data Availability Statement: The original contributions presented in this study are included in the article. Further inquiries can be directed to the corresponding author.

Conflicts of Interest: Authors Wanguo Zhang, Yuanshun Xiong, Yuanhui Qiao and Quansheng Sun were employed by the company China Railway 14th Bureau Group Co., Ltd., Jinan, China. The remaining authors declare that the research was conducted in the absence of any commercial or financial relationships that could be construed as potential conflicts of interest.

References

1. Dunant, F.C.; Joseph, S.; Prajapati, R.; Allwood, J.M. Electric recycling of Portland cement at scale. *Nature* **2024**, *629*, 1055–1061. [CrossRef] [PubMed]
2. Komnitsas, K.; Zaharaki, D. Geopolymerisation: A review and prospects for the minerals industry. *Miner. Eng.* **2007**, *20*, 1261–1277. [CrossRef]
3. Provis, J.L.; Palomo, A.; Shi, C.J. Advances in understanding alkali-activated materials. *Cem. Concr. Res.* **2015**, *78*, 110–125. [CrossRef]
4. Guang, Y. M&S highlight: Provis (2014), geopolymers and other alkali activated materials—Why, how, and what? *Mater. Struct.* **2022**, *55*, 113.
5. Brough, A.; Atkinson, A. Sodium silicate-based, alkali-activated slag mortars. *Cem. Concr. Res.* **2002**, *32*, 865–879. [CrossRef]
6. Zhang, J.; Yang, Y.; Li, X.; Chi, C.; Yang, Y. Alkali activation of industrial waste fly ash to produce high-value-added CSH seeds. *Adv. Cem. Res.* **2026**, *38*, 1–15. [CrossRef]
7. Tu, W.; Zhu, Y.; Fang, G.; Wang, X.; Zhang, M. Internal curing of alkali-activated fly ash-slag pastes using superabsorbent polymer. *Cem. Concr. Res.* **2019**, *116*, 179–190. [CrossRef]
8. Chilmon, K.; Woyciechowski, P.; Jaworska, B. The effect of CaO properties on the early volume change behavior, compressive strength and microstructure of CaO-activated GGBFS composites. *Case Stud. Constr. Mater.* **2025**, *23*, e05467. [CrossRef]
9. Tang, C.; Dong, R.; Tang, Z.; Long, G.; Ma, G.; Wang, H.; Huang, Y. Effect of SAP on the properties and microstructure of cement-based materials in the low humidity environment. *Case Stud. Constr. Mater.* **2024**, *20*, e03001. [CrossRef]
10. Han, Y.; Xie, Y.; Li, W.; Yue, Q.; Liu, Y.; Peng, B. Using SAP to control the deformation of shrinkage-compensating concretes at early age. *Constr. Build. Mater.* **2024**, *416*, 135139. [CrossRef]
11. Jingbin, Y.; Zhenping, S.; Nele, B.D.; Snoeck, D. Properties and Microstructure of Alkali-Activated Slag Paste Modified by Superabsorbent Polymers. *J. Mater. Civ. Eng.* **2024**, *36*, 04024072. [CrossRef]
12. Dong, B.; Qiu, Q.; Xiang, J.; Huang, C.; Sun, H.; Xing, F.; Liu, W. Electrochemical impedance interpretation of the carbonation behavior for fly ash–slag–cement materials. *Constr. Build. Mater.* **2015**, *93*, 933–942. [CrossRef]
13. Ann, Y.K.; Song, H. Chloride threshold level for corrosion of steel in concrete. *Corros. Sci.* **2007**, *49*, 4113–4133. [CrossRef]

14. Rostami, V.; Shao, Y.; Boyd, J.A. Microstructure of cement paste subject to early carbonation curing. *Cem. Concr. Res.* **2012**, *42*, 186–193. [CrossRef]
15. Law, W.D.; Adam, M.; Patnaikuni, I.; Wardhono, A. Long term durability properties of class F fly ash geopolymer concrete. *Mater. Struct.* **2015**, *48*, 721–731. [CrossRef]
16. Liu, J.; Qiu, Q.; Chen, X.; Wang, X.; Xing, F.; Han, N.; He, Y. Degradation of fly ash concrete under the coupled effect of carbonation and chloride aerosol ingress. *Corros. Sci.* **2016**, *112*, 364–372. [CrossRef]
17. Zhu, X.; Zi, G.; Cao, Z.; Cheng, X. Combined effect of carbonation and chloride ingress in concrete. *Constr. Build. Mater.* **2016**, *110*, 369–380. [CrossRef]
18. Badar, S.M.; Kupwade-Patil, K.; Bernal, A.S.; Provis, J.L.; Allouche, E.N. Corrosion of steel bars induced by accelerated carbonation in low and high calcium fly ash geopolymer concretes. *Constr. Build. Mater.* **2014**, *61*, 79–89. [CrossRef]
19. Davidovits, J. Geopolymers and geopolymeric materials. *J. Therm. Anal. Calorim.* **2005**, *35*, 429–441. [CrossRef]
20. Guo, Q.L.; Du, L.; Hua, L.; Gao, M.; Liu, R.; Ainisa, J. Study on properties of alkali-activated slag-steel slag composite cementitious system. *New Build. Mater.* **2024**, *51*, 108–113.
21. Ma, Y.; Ye, G.; Hu, J. Micro-mechanical properties of alkali-activated fly ash evaluated by nanoindentation. *Constr. Build. Mater.* **2017**, *147*, 407–416. [CrossRef]
22. Lv, Y.G.; Xiao, B.H.; Han, W.W.; Peng, H.; Qiao, J.; Wang, C.; Li, X. Research progress on carbonation performance of alkali-activated cementitious materials. *Sci. Technol. Rev.* **2022**, *40*, 94–104.
23. Bernal, S.A.; Provis, J.L.; Brice, D.G. Accelerated carbonation testing of alkali-activated binders significantly underestimates service life: The role of pore solution chemistry. *Cem. Concr. Res.* **2012**, *42*, 1317–1326. [CrossRef]
24. Bernal, A.S.; Provis, J.L.; Walkley, B.; San Nicolas, R.; Gehman, J.D.; Brice, D.G.; Kilcullen, A.R.; Duxson, P.; Van Deventer, J.S. Gel nanostructure in alkali-activated binders based on slag and fly ash, and effects of accelerated carbonation. *Cem. Concr. Res.* **2013**, *53*, 127–144. [CrossRef]
25. Perardt, M.; Angulski da Luz, C.; Pereira Filho, J.I.; Perardt, M.; Angulski da Luz, C.; Pereira Filho, J.I.; Ongaratto Trentin, P.; Alves de Medeiros, R., Jr. Improving the Carbonation Resistance of Alkali-Activated Slag Containing Mineral Additions: Investigation under Natural and Accelerated Conditions. *J. Mater. Civ. Eng.* **2025**, *37*, 4024518.1–4024518.14. [CrossRef]
26. Palacios, M.; Puertas, F. Effect of carbonation on alkali-activated slag paste. *J. Am. Ceram. Soc.* **2006**, *89*, 3211–3221. [CrossRef]
27. *GB/T 27973-2011*; Test Method for Fineness of Mineral Admixtures. Standards Administration of the People's Republic of China: Beijing, China, 2011.
28. *GB/T 18046-2008*; Ground granulated blast furnace slag used for cement and concrete. Standards Administration of the People's Republic of China (SAC): Beijing, China, 2008.
29. *GB/T 1596-2017*; Fly ash used for cement and concrete. Standards Administration of the People's Republic of China (SAC): Beijing, China, 2017.
30. Lin, J.; Wang, S.; Yu, H.; Ye, S.; Mao, J.; Chen, S.; Liu, Y.; Yan, D. Carbonation property analysis and carbonation process modeling of GGBFS-based foam alkali-activated binder. *Cem. Concr. Compos.* **2026**, *167*, 106446. [CrossRef]
31. Xu, Y.J.; Li, S.S.; Zhang, J.; Ghafoor, M.T.; Hu, X.; Shi, C. Effect of reactive magnesium oxide on hydration and microstructural evolution of alkali-activated slag cement. *J. Chin. Ceram. Soc.* **2025**, *53*, 3136–3157.
32. Wang, H.Q.; Fan, H.; Niu, B.L.; Wan, X.M. Review on carbonation of alkali-activated concrete. *Concrete* **2025**, *2*, 13–20.
33. Tian, J.W.; Song, B.B.; Liu, Z.M. Superabsorbent polymer in alkali-activated slag paste: Swelling-deswelling behaviour and effects on surrounding matrix. *Cem. Concr. Compos.* **2024**, *146*, 105365.
34. Gökçe, S.H. Durability of slag-based alkali-activated materials: A critical review. *J. Aust. Ceram. Soc.* **2024**, *60*, 885–903. [CrossRef]
35. Wang, J.Z. Study on Mechanical and Carbonization Properties of Alkali-Activated Slag-Fly ash Geopolymer. Master's Thesis, Changsha University of Science & Technology, Changsha, China, 2023.
36. Zhao, Y.Q. Research on the Impact of Calcium Carbide Slag-Based Activator on the Hydration and Rheological Properties of Alkali-Activated Slag Cement. Ph.D. Thesis, Northeastern University, Shenyang, China, 2023.
37. Chang, J.; Fang, Y.F.; Shang, X.P.; Wang, J.R. Effect of accelerated carbonation on microstructure of calcium silicate hydrate. *J. Chin. Ceram. Soc.* **2015**, *43*, 1055–1060.
38. Da, Y.; Laixue, P.; Di, S.; Mingyang, L.; Jiabin, W.; Zebin, G. Reaction Mechanism of Fly Ash in Alkali-Activated Slag/Fly Ash System. *Bull. Chin. Ceram. Soc.* **2021**, *40*, 3005.
39. Nedeljković, M.; Ghiassi, B.; Melzer, S.; Kooij, C.; van der Laan, S.; Ye, G. CO_2 binding capacity of alkali-activated fly ash and slag pastes. *Ceram. Int.* **2018**, *44*, 19646–19660. [CrossRef]
40. Harirchi, P.; Yang, M.J. Exploration of Carbon Dioxide Curing of Low Reactive Alkali-Activated Fly Ash. *Materials* **2022**, *15*, 3357. [CrossRef]
41. Zhang, J.; Shi, C.J.; Zhang, Z.H. Carbonation induced phase evolution in alkali-activated slag/fly ash cements: The effect of silicate modulus of activators. *Constr. Build. Mater.* **2019**, *223*, 566–582. [CrossRef]

42. Li, X.G.; Xu, J.S.; Jiang, D.B.; Lyu, Y.; He, C.; Zhang, C.; Fu, Q. Effect of SAP internal curing on properties of alkali-activated slag cementitious materials. *Bull. Chin. Ceram. Soc.* **2021**, *40*, 3435–3441. [CrossRef]
43. Abd El Haleem, W.M.; Soliman, A.S. Synergetic effect of superabsorbent polymer and shrinkage reducing admixture on the properties of alkali-activated slag binders. *J. Build. Eng.* **2023**, *79*, 107786. [CrossRef]
44. Jiang, D.B.; Li, X.G.; Yang, L.; Li, C.; Jiang, W.; Liu, Z.; Xu, J.; Zhou, Y.; Dan, J. Autogenous shrinkage and hydration property of alkali activated slag pastes containing superabsorbent polymer. *Cem. Concr. Res.* **2021**, *149*, 106581. [CrossRef]
45. Yuan, Y.; Zhao, R.D.; Zhan, Y.L.; Li, F.; Cheng, Z.; Li, J. Carbonation resistance of fly ash-slag based geopolymer concrete. *J. Southwest Jiaotong Univ.* **2021**, *56*, 1275–1282.

Disclaimer/Publisher's Note: The statements, opinions and data contained in all publications are solely those of the individual author(s) and contributor(s) and not of MDPI and/or the editor(s). MDPI and/or the editor(s) disclaim responsibility for any injury to people or property resulting from any ideas, methods, instructions or products referred to in the content.